



# A general study of counterflow diffusion flames at subcritical and supercritical conditions: Oxygen/hydrogen mixtures



Hongfa Huo<sup>1</sup>, Xingjian Wang, Vigor Yang\*

School of Aerospace Engineering, Georgia Institute of Technology, Atlanta, GA 30332, United States

## ARTICLE INFO

### Article history:

Received 8 January 2014

Received in revised form 24 April 2014

Accepted 5 June 2014

Available online 10 July 2014

### Keywords:

Supercritical combustion

Counterflow diffusion flame

S-curve

Real fluids

Strain rate

Tabulated chemistry

## ABSTRACT

A theoretical framework is established to study the effect of flow strain rate on counterflow diffusion flames for general fluids over the entire thermodynamic regime. The formulation accommodates fundamental thermodynamics and transport theories, along with detailed chemical mechanisms. Both steady and unsteady burning branches of a complete flame-response curve (the S-curve) are considered. An improved two-point flame-controlling continuation method is employed to solve the singularity problem at the turning points on the S-curve. As a specific example, oxygen/hydrogen flames are systematically investigated over a pressure range of 0.5–200 atm. The strain rate is varied from  $10^2$  to  $10^8$  s<sup>-1</sup>. Two different inlet temperatures for oxygen (120 and 300 K) and hydrogen (20 and 300 K) are treated to explore flame behaviors at the ideal-gas and cryogenic-liquid states. General flame similarities (in terms of flame temperature, flame thickness, species concentrations, reaction rates, and heat release rate) are developed in a normalized strain-rate space ( $a/a_{ext}$ ) for the entire range of pressures under consideration. Quantitative mapping of flame properties from one pressure to another is obtained. In addition, an analytical model is developed to refine and elucidate a previously established relationship between the heat release rate and pressure and strain rate in the form of  $\dot{q} \sim p^{0.534} \sqrt{a}$ . The heat release rate, when normalized with respect to  $p^{0.534} \sqrt{a_{ext}}$ , correlates well with the normalized strain rate ( $a/a_{ext}$ ). Both numerical and analytical results show that the extinction strain rate is approximately proportional to pressure; this allows for *a priori* mapping of flame solutions between different pressure conditions. This in turn will significantly improve the computational efficiency of combustion modeling using tabulated chemistry, including the flamelet, FGM, and FPI models. Cryogenic inlet temperature affects only the flame location, without discernibly modifying the flame structures, which suggests that the ideal-gas flame solutions can be used for flame tabulation.

© 2014 The Combustion Institute. Published by Elsevier Inc. All rights reserved.

## 1. Introduction

Laminar counterflow flames have been extensively studied under different flow and boundary conditions, due to their geometrical simplicity, fundamental flame behaviors and burning properties. When the flame temperature or burning rate (or any variable that characterizes the completeness of reactions, such as mass fractions of major combustion products) of a reactive system is plotted as a function of the corresponding Damköhler number (or any variable that measures the strength of external flow stretching, such as the strain rate or scalar dissipation rate), an S-shaped relationship, commonly known as an S-curve, is obtained. This phenomenon can be attributed to the exponential dependence of the

chemical reaction rate on temperature [1,2]. Here, the Damköhler number is defined as the ratio of the flow time scale to the chemical time scale. An S-curve covers all the possible steady chemical states that a given reacting mixture can achieve. It also reflects the response of a given chemical state to changes in the local aerothermal condition in a flame zone. An S-curve can thus be used to characterize the evolution of a flame subject to continually varying flow conditions, including ignition, extinction, and instability [3,4].

Figure 1 shows a schematic diagram of an S-curve. The zero Damköhler number ( $Da$ ) condition represents the frozen limit, corresponding to pure mixing of reactants. Along the lower branch (the weakly reacting flow branch), the chemical reaction rate increases with the  $Da$  number. Ignition occurs at  $Da = Da_{ign}$ , where the heat generation exceeds the heat loss in a steady state [1]. The flame temperature increases suddenly and takes a value in the upper branch. The reaction-sheet limit is attained as the  $Da$  number approaches infinity. When the  $Da$  number is progressively

\* Corresponding author. Fax: +1 404 894 2760.

E-mail address: [vigor@gatech.edu](mailto:vigor@gatech.edu) (V. Yang).

<sup>1</sup> Current address: GE Global Research Center, Niskayuna, NY, United States.

### Nomenclature

$a$	strain rate; parameter in the equation of state
$b$	parameter in the equation of state
$C$	scaling constant
$C_p$	specific heat capacity
$D$	mass diffusivity
$F, G, H$	functions of $x$ coordinate
$G(p)$	Gaussian distribution for pressure at $p$
$h$	specific enthalpy
$L$	distance between the counterflow inlets
$\dot{m}$	mass flow rate
$MW$	molecular weight
$p$	pressure
$\dot{q}$	heat release rate
$r$	radial coordinate
$R_u$	universal gas constant
$T$	temperature
$V$	diffusion velocity
$x$	$x$ coordinate
$Y$	mass fraction

### Greek symbols

$\alpha$	parameter in the equation of state
$\delta$	flame thickness
$\lambda$	thermal conductivity
$\mu$	dynamic viscosity; mean in the Gaussian distribution
$\rho$	density
$\sigma$	standard deviation in the Gaussian distribution
$\omega$	reaction rate

### Subscripts

$ext$	extinction point
$F$	fuel stream
$fix$	fixed location
$J$	grid index
$k$	the $k$ th species component
$L$	largest over the entire $S$ -curve; left side of the maximum flame temperature
$O$	oxidizer stream
$R$	right side of the maximum flame temperature
$S$	smallest over the entire $S$ -curve

decreased along the upper branch, the flame is extinguished at  $Da = Da_{ext}$ . Along the unstable middle branch, the flame temperature decreases with increasing  $Da$  number, a situation considered unphysical. The  $S$ -curve becomes monotonic, with a unique solution when the activation energy is smaller than a critical value [5]. Such a condition, however, is unlikely to occur in most practical systems, because of the large activation energies for common fuels.

Linan [5] performed an asymptotic analysis of counterflow diffusion flames using a one-step reaction mechanism over various segments of the  $S$ -curve: the frozen ignition regime, the partial burning regime, the premixed flame regime, and the near-equilibrium regime. Numerical methods were later developed to study one-dimensional counterflow flames with detailed chemical mechanisms [6–8]. These studies, however, focused only on the upper branch of the  $S$ -curve. Giovangigli and Smooke [9] applied the arc-length continuation method of Keller [10] in flame calculations to solve the singularity problem at the extinction point, and generated a complete  $S$ -curve. An alternative method, known as

the flame-controlling method, was proposed by Nishioka et al. [11] to treat the same problem. Recently, the FlameMaster code [12] and the CHEMKIN-PRO package [13], using the arc-length approach and the flame-controlling method, respectively, were developed to study the flame response throughout the entire  $S$ -curve. Those studies, however, are limited to ideal gases.

Many practical combustion devices operate at pressures well above the thermodynamic critical points of injected fuels [14]. Ribert et al. [15] incorporated general fluid properties into an existing code (DMCFs) [16] to investigate counterflow diffusion flames of hydrogen and oxygen in the pressure range of 10–250 atm. Both subcritical and supercritical conditions for the steady-burning branch of the  $S$ -curve were considered. Phenomenological dependence of the heat release rate on pressure and strain rate was established in the form of  $\dot{q} \sim \sqrt{pa}$ . Cryogenic inlet temperatures were also discussed for a fixed pressure and strain rate, and the pressure dependence of the extinction strain rate was explored. Following an approach similar to that reported in Ref. [15], Pons et al. [17] investigated the mass transfer and combustion in transcritical non-premixed counterflows of oxygen and methane in the pressure range of 60–200 atm.

Recently, Lacaze and Oefelein [18] have performed two-dimensional simulations of opposed jet flames of oxygen and hydrogen at supercritical pressures. Results were benchmarked against those in Ref. [15]. Similar observations were made of the effects of inlet temperature, pressure, and strain rate on the flame properties. Supercritical flames in the pressure range of 53–90 atm with strain rates of  $5 \times 10^4$ – $5 \times 10^6 \text{ s}^{-1}$  were found to exhibit very limited variation in flame temperature ( $\pm 3\%$ ) and major species profiles in the mixture-fraction space. A chemistry tabulation model was developed to reproduce the flame results with detailed chemistry.

The studies described here ([15,17,18]) considered only the upper branch of the  $S$ -curve. The extinction point was not identified, due to numerical challenges. No flame solution beyond the extinction point was obtained, and the behavior of the unstable burning branch of the  $S$ -curve was not investigated.

The present study attempts to develop a general framework based on the analysis described in [15]. Within this general framework, the flame solution for real fluids would be obtained over a complete  $S$ -curve with detailed chemical mechanisms. Results will

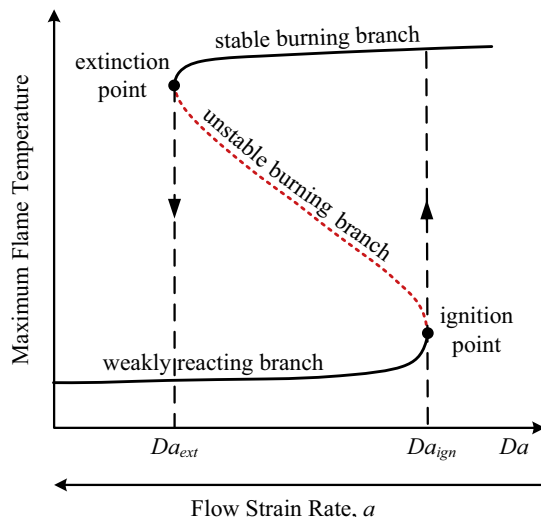


Fig. 1. Schematic diagram of a folded  $S$ -shaped flame response.

shed light on flame behaviors over the entire fluid thermodynamic regime, from compressed liquid to ideal gas through the transcritical state. Results can also be implemented to generate chemistry tables for supercritical combustion models using tabulated chemistry, such as the flamelet approach in [19]. As a specific example, oxygen/hydrogen counterflow diffusion flames are explored systematically in the pressure range of 0.5–200 atm. The inlet temperatures of oxygen and hydrogen considered here are between 120–300 K and 20–300 K, respectively. Detailed information about the flame structures and heat release characteristics is obtained for strain rates of  $10^2$ – $10^8$  s $^{-1}$ . The major contributions of the present study include: (1) flame solutions for real fluids are extended to the entire *S*-curve; (2) a theoretical analysis is derived from the conservation equations to quantify the dependence of the heat release rate on pressure and strain rate, as well as the effect of pressure on the extinction strain rate; and (3) general flame similarities are established in a normalized strain-rate space for the flame temperature, flame thickness, species concentrations, reaction rates, and heat release rate.

## 2. Theoretical formulation

Figure 2 shows the physical model of concern, a counterflow diffusion flame produced by two opposed fluid jets issuing from two circular nozzles [15,18]. The configuration produces an axisymmetric laminar flowfield with a stagnation plane in the middle. The theoretical formulation for this type of flames has been well established for ideal gases [9,11]. The present study extends previous analyses by incorporating general-fluid thermodynamics and transport theories, such that a unified framework can be constructed to treat the flame response for real fluids over a complete *S*-curve, including both the steady- and unstable-burning branches.

### 2.1. Governing equations

The governing equations for steady-state axisymmetric problems are reduced to a set of ordinary differential equations, following Refs. [7,15].

Continuity:

$$G(x) - \frac{dF(x)}{dx} = 0, \quad (1)$$

where *F* is introduced with a stream function to convert the original partial differential equations to ordinary differential equations.

Radial momentum:

$$H - 2 \frac{d}{dx} \left( \frac{FG}{\rho} \right) + \frac{3G^2}{\rho} + \frac{d}{dx} \left[ \mu \frac{d}{dx} \left( \frac{G}{\rho} \right) \right] = 0, \quad (2)$$

where  $\mu$  is the molecular viscosity. *H* is defined as

$$H = \frac{1}{r} \left( \frac{\partial p}{\partial r} \right) = \text{constant}. \quad (3)$$

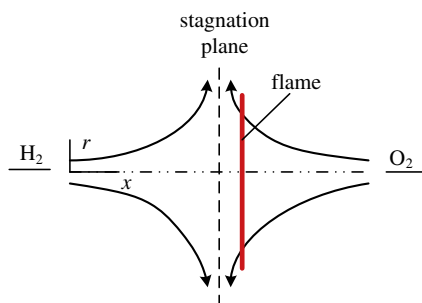


Fig. 2. Schematic diagram of a counterflow diffusion flame.

Energy:

$$2F \sum_{k=1}^K Y_k \frac{\partial \hat{h}_k}{\partial x} - \frac{d}{dx} \left( \lambda \frac{dT}{dx} \right) + \rho \sum_{k=1}^K Y_k V_k \frac{\partial \hat{h}_k}{\partial x} + \sum_{k=1}^K MW_k \hat{h}_k \dot{\omega}_k = 0. \quad (4)$$

Species:

$$2F \frac{dY_k}{dx} + \frac{d}{dx} (\rho Y_k V_k) - \dot{\omega}_k MW_k = 0, \quad k = 1, \dots, K, \quad (5)$$

where the partial-mass enthalpy of species *k*,  $\hat{h}_k$  is calculated based on fundamental thermodynamics theories to account for real-fluid effects [20]. At the ideal-gas limit,  $d\hat{h}_k = C_{p,k} dT$ , with  $C_{p,k}$  being the specific heat capacity of species *k*. The energy equation then degenerates to the version given in Ref. [7].

### 2.2. Equation of State (EOS) and thermophysical properties

An equation of state is needed to close the formulation. The present work features a unified treatment of thermodynamic and transport properties and can accommodate any equation of state. As a specific example, the Soave–Redlich–Kwong (SRK) equation of state is used because of its reasonable accuracy for a wide range of fluid states, easy implementation, and extensive applications in the study of supercritical mixing and combustion [15,17,20–23]. The SRK equation of state takes the form:

$$p = \frac{\rho R_u T}{MW - b\rho} - \frac{a\alpha}{MW} \frac{\rho^2}{MW + b\rho}, \quad (6)$$

where  $R_u$  is the universal gas constant and  $\alpha$  is a model parameter given in [24]. *a* and *b* account for attractive and repulsive forces between molecules, respectively.

Full account is taken of general-fluid thermodynamics and transport over the entire temperature and pressure regimes of concern. The thermodynamic properties, such as enthalpy, Gibbs energy, and specific heat capacity, are derived directly from fundamental thermodynamic theories. They are expressed as the sum of an ideal-gas property at the same temperature and a thermodynamic departure function accounting for dense-fluid correction [14]. Transport properties, such as viscosity and thermal conductivity, are estimated using the method of Chung et al. [25]. The binary mass diffusivity is obtained by the Takahashi method calibrated for high pressure conditions [26]. The implementation and validation of the property evaluation schemes are outlined in [14,27].

### 2.3. Boundary conditions

Boundary conditions must be specified properly. Two types of boundary conditions are typically applied. Dixon–Lewis et al. [6] assumed a stagnation-point potential flow at the boundaries by linearly correlating the radial and axial velocities with a constant strain rate. Kee et al. [7] considered a uniform (plug) flow at the nozzle exit by specifying zero radial velocity. Chelliah et al. [8] showed that the plug-flow boundary condition is more suitable for counterflow burners. It is thus employed in the present study.

At the fuel inlet,

$$F = \frac{\rho_F u_F}{2}, \quad G = 0, \quad T = T_F, \quad \rho u Y_k + \rho Y_k V_k = (\rho u Y_k)_F. \quad (7)$$

At the oxidizer inlet,

$$F = \frac{\rho_O u_O}{2}, \quad G = 0, \quad T = T_O, \quad \rho u Y_k + \rho Y_k V_k = (\rho u Y_k)_O, \quad (8)$$

where the subscripts *F* and *O* denote the fuel and oxidizer streams, respectively. The distance between the two inlets is fixed to

$L = 2$  cm, with the fuel inlet at  $x = 0$  and the oxidizer inlet at  $x = L$ . It is worth noting that the velocity boundary condition in [15,18] is specified in such a manner that its gradient corresponds to the strain rate of concern. The strain rate in the current work, however, is treated as an eigenvalue of the numerical system, not an input parameter.

#### 2.4. Numerical methods

The governing equations can be written in the following vector form,

$$L(\phi) = 0, \quad (9)$$

where  $\phi = \phi(F_{J=1}, G_{J=1}, H_{J=1}, T_{J=1}, Y_{k,J=1}, \dots, F_{J=N}, G_{J=N}, H_{J=N}, T_{J=N}, Y_{k,J=N})$  includes all primary variables at the grid points and  $L$  is a differential operator. The subscript  $J$  is the grid index and  $N$  is the number of grid points. For a given chemical mechanism involving  $K$  species, the total number of differential equations is  $N(K+3)$ . A modified Newton iteration method is implemented to solve these equations.

Formulation (9) represents a well-posed two-point boundary-value problem. The flame solution along the steady branch of the S-curve has been previously obtained for ideal gases [9,11] and real fluids [15,17]. When the strain rate reaches its extinction limit, a numerical singularity appears, leading to a serious difficulty in

convergence. A two-point flame-controlling continuation method [11] is employed to overcome this challenge, as illustrated in Fig. 3. Given an initial solution denoted by the solid line in Fig. 3a, two control points ( $X_L, X_R$ ) are selected on both sides of the peak temperature, with known temperature values ( $T_L, T_R$ ). Application of a temperature change at the two control points gives rise to a new flame solution denoted by the dashed line. The temperature changes are negative in Fig. 3a, that is,  $\Delta T_L < 0$  and  $\Delta T_R < 0$ . As a result, the maximum flame temperature decreases while the fuel inlet velocity and strain rate increase. Fig. 3b shows typical numerical results. The maximum flame temperature continues to decrease and finally reaches a critical point where extinction occurs, corresponding to  $Da_{ext}$  as shown in Fig. 1. Near the extinction point, further decreases in the temperatures at the two controlling points result in a monotonic decrease in the maximum flame temperature. The flame solution then moves smoothly from the upper branch to the middle branch.

Since two internal boundary conditions have been applied at the controlling points, two boundary conditions must be released to render the governing equations well posed. In the present work, dummy equations are added for  $H$  and  $u_F$  at every grid point except the two controlling points. The mathematical formulation follows.

At controlling point  $X_L$ ,

$$\frac{dH}{dx} = 0, \quad J \neq J_{R,fix}; \quad T[J] = T_R, \quad J = J_{R,fix}. \quad (10)$$

At controlling point  $X_R$ ,

$$\frac{du_F}{dx} = 0, \quad J \neq J_{L,fix}; \quad T[J] = T_L, \quad J = J_{L,fix}, \quad (11)$$

where the subscripts  $R$  and  $L$  denote the control points on the right and left hand sides of the flame, respectively. The subscript *fix* denotes a fixed point in the flowfield.

### 3. Results and discussion

The theoretical and numerical framework outlined above is used to study the S-curve response of hydrogen–oxygen counterflow diffusion flames over a broad range of pressures and strain rates. The chemical kinetic mechanism developed by Li et al. [28] is employed; it consists of 8 species ( $H_2, H, O, O_2, OH, HO_2, H_2O, H_2O_2$ ) and 19 reversible elementary reactions. This mechanism has been validated against experimental data for shock tubes, flow reactors and laminar premixed flames over a temperature range of 298–3000 K, a pressure range of 0.3–87 atm, and an equivalence ratio range of 0.25–5.0. It should be noted that the present study covers pressures up to 200 atm, and flame temperatures over 3000 K. An improved kinetics scheme is warranted for higher pressures and temperatures. For reference, the critical pressures and temperatures for oxygen and hydrogen are listed in Table 1.

#### 3.1. Model validation

As part of model validation, a hydrogen–oxygen counterflow diffusion flame at 1 atm is first considered. The strain rate, defined based on the maximum velocity gradient on the fuel side [8], is  $a = 500 \text{ s}^{-1}$ . The inlet temperatures are fixed at 300 K. Four different approaches are employed. The baseline case is an ideal-gas approach modeled using the CHEMKIN package. Case II employs

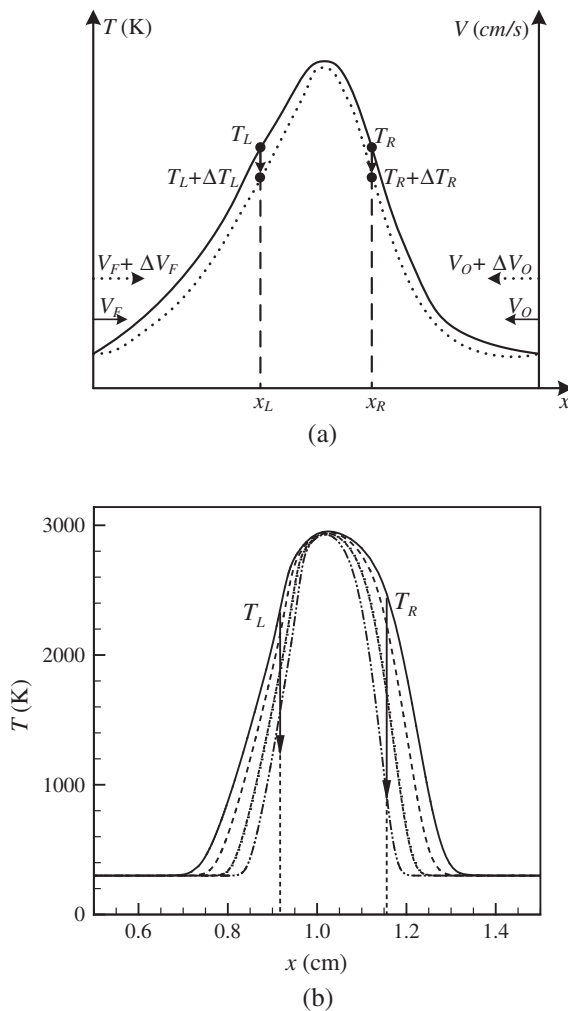


**Fig. 3.** (a) Schematic of two-point temperature-controlling continuation method, solid line: initial solution, dashed line: new solution; (b) changes of temperature distribution applying two-point temperature-controlling method, solid line:  $V_F = 105$  cm/s, dashed line: 136 cm/s, dash-dotted line: 200 cm/s, dash-dot-dotted line: 301 cm/s.

**Table 1**

Critical points of hydrogen and oxygen.

Reactants	$T_{cr}$ , K	$p_{cr}$ , bar	$V_{cr}$ , cm <sup>3</sup> /mol
H <sub>2</sub>	33.25	12.97	65.00
O <sub>2</sub>	154.58	50.43	73.37

the SRK EOS with ideal-gas property evaluation. Case III incorporates the SRK EOS and real-fluid thermodynamics. Case IV accommodates a full treatment of real fluids, including the SRK EOS, thermodynamic, and transport properties. Figure 4 shows the temperature profiles obtained from the four different approaches. They are nearly identical for the first three cases with a maximum flame temperature of 3022 K. For Case IV, the flame shape is slightly different in the fuel-rich region, and the maximum flame temperature is 11 K higher. The difference appears to be negligible. Results indicate that the SRK EOS and real-fluid property evaluation schemes are implemented properly. The fluid behavior at the ideal-gas limit is recovered accurately. Although not shown here, flame structure results from the present numerical scheme and the CHEMKIN code are almost identical in terms of species and heat release distributions. Such close agreement validates the present analysis.

The property evaluation scheme must be examined carefully. Fluids often experience thermodynamic and transport anomalies when they are injected from a compressed-liquid state into an environment where the temperature and pressure exceed their critical values, especially at pressures close to the critical point [14]. Figure 5 plots thermophysical properties showing good agreement with the NIST database for oxygen at 100 atm, over a temperature range covering both the subcritical and supercritical regimes.

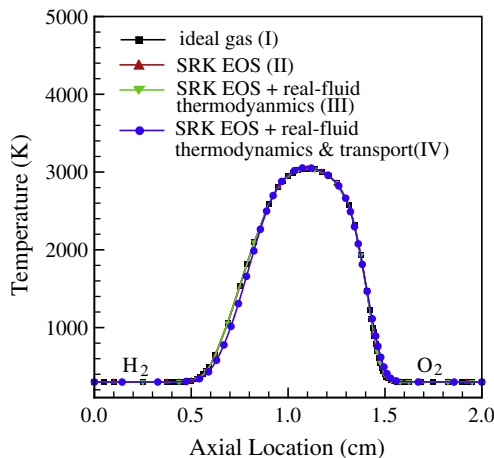


Fig. 4. Temperature distributions at  $p = 1$  atm,  $T_{H_2} = T_{O_2} = 300$  K, and  $a = 500$  s $^{-1}$ .

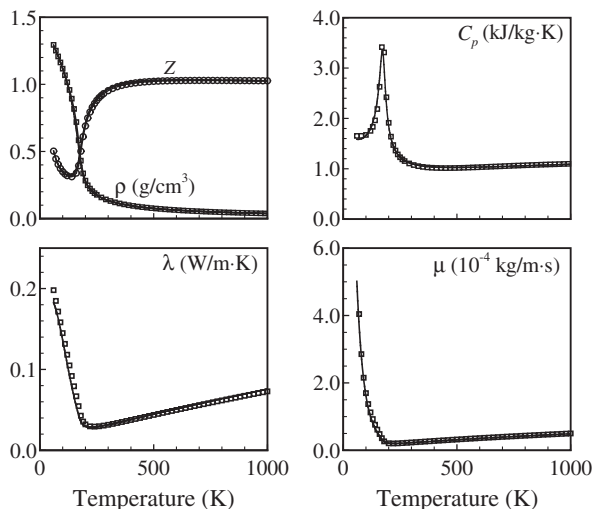


Fig. 5. Validation of thermodynamic and transport properties of oxygen against NIST data.  $p = 100$  atm. Lines: the present numerical scheme; symbols: NIST data. Compressibility ( $Z$ ) and density ( $\rho$ ), specific heat at constant pressure ( $C_p$ ), thermal conductivity ( $\lambda$ ), and dynamic viscosity ( $\mu$ ).

The compressibility factor is significantly smaller than unity at low temperatures, which is not the case for the ideal gas condition.

### 3.2. S-curve flame response

The flame response to the variation of the flow strain rate is investigated over a broad pressure range of 0.5–200 atm. The inlet temperatures of oxygen and hydrogen vary from 120–300 K to 20–300 K, respectively. The flame characteristics over the entire fluid thermodynamic regime, from compressed liquids to ideal gases, are examined systematically. As an example, Fig. 6 shows the temperature profiles at 50 atm with a strain rate of 10,004 s $^{-1}$ . Significant differences between the results of the ideal-gas (I) and real-fluid (IV) approaches are observed.

#### 3.2.1. Effect of pressure and strain rate

Figure 7 shows the maximum flame temperature as a function of strain rate at various pressures. The solid and dashed lines are real-fluid and ideal-gas (CHEMKIN) results, respectively. They match closely. The weakly reacting (lower) branch shown schematically in Fig. 1 is not present here, due to the low inlet temperature of 300 K, which is well below the ignition point. A complete S-curve response can be obtained with a higher inlet temperature [11]. The maximum flame temperature remains almost constant at low strain rates, and starts to decrease progressively until the extinction point is reached. At low strain rates, the  $Da$  number is large. Chemical reactions have sufficient time to release thermal energy to balance heat loss. Further increase in the strain rate

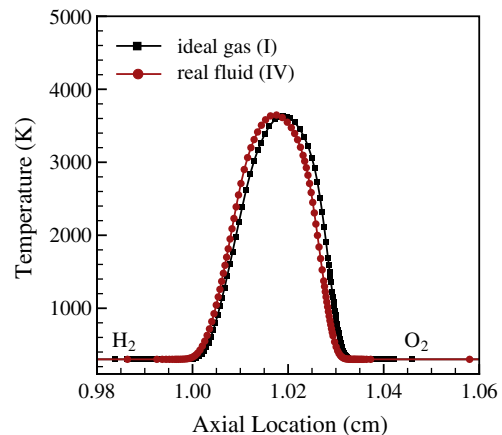


Fig. 6. Temperature distributions at  $p = 50$  atm,  $T_{H_2} = T_{O_2} = 300$  K, and  $a = 10,004$  s $^{-1}$ .

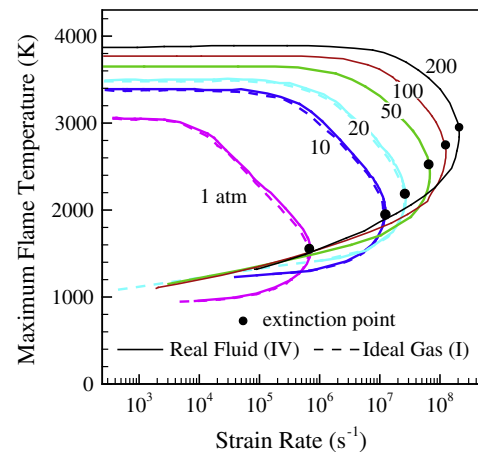


Fig. 7. Maximum flame temperatures at various pressures,  $T_{H_2} = T_{O_2} = 300$  K.

renders the flow residence time comparable to the chemical reaction time. The resultant incomplete combustion results in a lower flame temperature. The heat generation eventually reaches a point that cannot overcome the heat loss; the flame comes to a sharp extinction. For a given strain rate, the maximum flame temperature always increases with increasing pressure.

Figure 8 shows the effect of strain rate at various pressures on the total heat release rate per unit area, defined as

$$\dot{q} = \int_0^L \left( \sum_{k=1}^K \hat{h}_k MW_k \dot{\omega}_k \right) dx. \quad (12)$$

A linear relationship is observed on log–log scales. Along the stable burning (upper) branch, the heat release rate first increases linearly with the strain rate, then reaches a maximum (indicated with dots in Fig. 8), and finally decreases, before the flame is extinguished. At the extinction point, the variation of the heat-release rate with respect to the strain rate becomes infinite, producing a mathematical singularity. Further decrease of the strain rate beyond this point reduces the heat release rate. The unstable burning (lower) branch shows an inverse behavior as compared to the upper branch. This result appears to be the first of its kind obtained beyond the extinction limit for high-pressure conditions using a real-fluid approach.

The heat-release rate profiles indicate a strong similarity for different pressures. Careful data analysis shows that the heat-release rate in the upper (stable burning) branch of the S-curve can be correlated with pressure and strain rate  $a$  as  $\dot{q} \sim \sqrt{pa}$ . The same relationship was previously obtained by Ribert et al. [15] and Lacaze and Oefelein [18], but the physical meaning of the relationship has not yet been clearly explained. In addition, the pressure effects on the maximum flame temperature and species concentrations are yet to be addressed. A theoretical analysis is thus developed in the present study by means of the energy and species conservation, in order to provide direct insight into observed phenomena.

When the strain rate is significantly smaller than the extinction value,  $a_{ext}$  (that is, the flow time is much greater than its chemical counterpart and the  $Da$  number is large), the flame is diffusion-controlled. An order of magnitude analysis of the energy conservation in Eq. (4) shows that the heat flux is primarily driven by conduction rather than mass diffusion. Furthermore, these two terms are greater than the convection term by at least two orders of magnitude. Both findings are corroborated by the present numerical results. With the neglect of higher-order terms, the energy balance between heat production and heat loss by conduction becomes

$$\frac{d}{dx} \left( \lambda \frac{dT}{dx} \right) - \sum_{k=1}^K MW_k \hat{h}_k \dot{\omega}_k \approx 0. \quad (13)$$

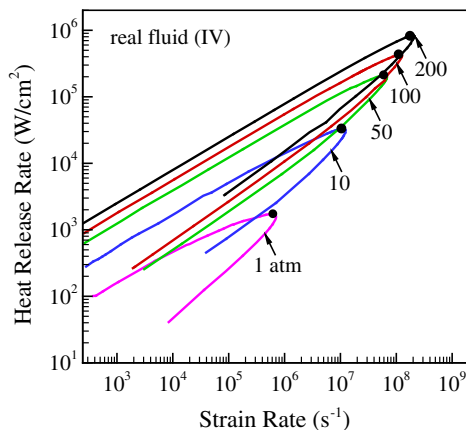


Fig. 8. Heat release rate per unit area as function of strain rate:  $p = 1$ –200 atm,  $T_{H_2} = T_{O_2} = 300$  K.

Integrating Eq. (13) throughout the flame zone, we have

$$\dot{q} = \sum_{k=1}^K \int_0^L MW_k \hat{h}_k \dot{\omega}_k dx \cong \bar{\lambda} \frac{\bar{T}}{\delta^2} \delta, \quad (14)$$

where  $\bar{\lambda}$  is the average thermal conductivity,  $\bar{T}$  the mean temperature in the flame zone, and  $\delta$  the flame thickness. The left-hand side of Eq. (14) represents the rate of chemical energy release per unit flame area. In a diffusion-controlled flame,  $MW_k \dot{\omega}_k$  in the species equation, Eq. (5), is determined by the molecular diffusion process represented by  $d(\rho Y_k V_k)/dx$ , with the convection term  $\rho u dY_k/dx$  being an order of magnitude smaller. A dimensional analysis suggests that  $d(\rho Y_k V_k)/dx \sim \rho D/\delta^2$ . Assuming a Lewis number of unity, the thermal diffusivity,  $\alpha = \lambda/(\rho C_p)$ , becomes identical to the mass diffusivity  $D$ . In the flame zone,  $\hat{h}_k \sim C_p \bar{T}$ . Substitution of these terms into the left hand side of Eq. (14) gives  $q \sim \bar{\lambda} \bar{T}/\delta$  which is the same as the right hand side of Eq. (14). The thermal conductivity varies with temperature as  $\bar{\lambda} \sim \sqrt{\bar{T}/MW_{mix}}$ . The right hand side of Eq. (14) becomes  $\bar{T}^{1.5}/(\delta \sqrt{MW_{mix}})$ . The flame thickness can be correlated with the mass diffusivity and strain rate as  $\delta \sim \sqrt{D/a}$  [2], where the mass diffusivity  $D$  depends on temperature and pressure in the form of  $D \sim \bar{T}^{1.5}/(p \sqrt{MW_{mix}})$ , according to gas kinetics theories [29]. Incorporation of the above expressions into Eq. (14) leads to

$$\dot{q} \sim \frac{\bar{T}^{0.75}}{MW_{mix}^{0.25}} \sqrt{pa}. \quad (15)$$

This relationship was previously derived by Poinot and Veynante [30] based on assumptions of infinitely fast chemistry and constant density. The present study addresses this issue from a different perspective. For a given reactive system, the flame temperature and mixture molecular weight are relatively insensitive to pressure. Eq. (15) reduces to  $\dot{q} \sim \sqrt{pa}$  and recovers the phenomenological correlation introduced by Ribert et al. [15]. The present work provides a theoretical basis for the heat-release relationship with pressure and strain rate.

As indicated by Fig. 7, the maximum flame temperature at low strain rates depends weakly on pressure as  $\bar{T} \sim p^{0.045}$ . The mixture molecular weight changes slightly with the strain rate and pressure, with the maximum deviation being less than 20% over the conditions of concern. It is thus assumed to remain constant to first approximation. Eq. (15) becomes

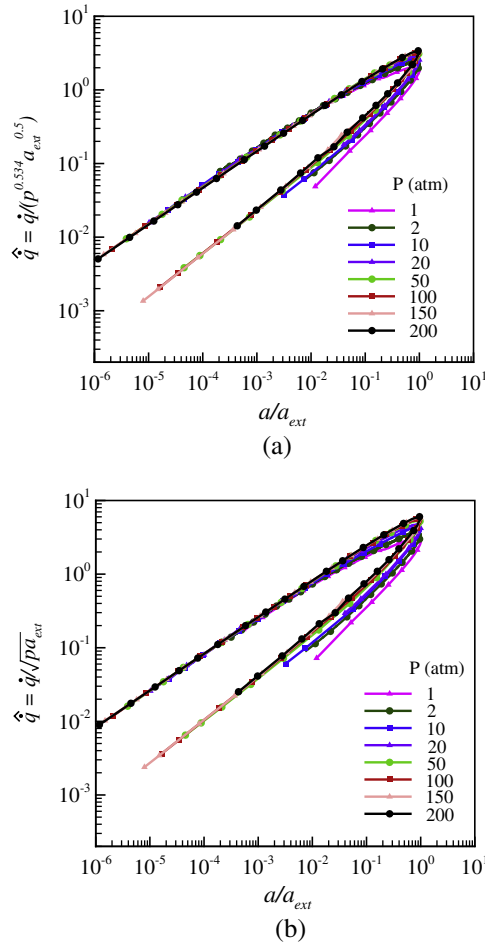
$$\frac{\dot{q}}{p^{0.534}} \sim \sqrt{a}. \quad (16)$$

Normalization of the strain rate by its extinction value,  $a_{ext}$ , gives

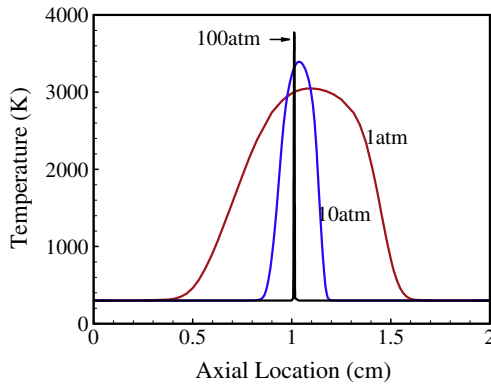
$$\frac{\dot{q}}{p^{0.534} a_{ext}^{0.5}} \sim \sqrt{\frac{a}{a_{ext}}}. \quad (17)$$

Figure 9a shows the scaled heat release rate,  $\hat{q} \equiv \dot{q}/(p^{0.534} a_{ext}^{0.5})$ , as a function of the reduced strain rate,  $a/a_{ext}$ . All the curves collapse to a single profile. The correlation works well even near the extinction point, especially for pressures greater than 2 atm. The same information with a simplified version of the scaled heat release,  $\hat{q} \equiv \dot{q}/\sqrt{pa_{ext}}$ , is given in Fig. 9b. The difference between the two scaled heat releases appears to be quite modest, although Eq. (17) offers slightly improved agreement. The importance of the present analysis is twofold: (1) the physical basis for the heat-release dependence on pressure and strain rate is established directly from the conservation laws, and (2) a general correlation for the heat-release rate is obtained.

The general correlation for heat release in Eq. (17) suggests that the flame behaviors at high pressures can be predicted based on those at low pressures. To further clarify the existence of such a flame similarity, results for the flame thickness, temperature,



**Fig. 9.** Scaled heat release rate  $\hat{q}$  as function of normalized strain rate ( $a/a_{ext}$ ). (a) New scale, Eq. (17); (b) old scale,  $\hat{q} = \dot{q} / \sqrt{p a_{ext}}$ .



**Fig. 10.** Temperature profile at different pressures and strain rates, 1 atm  $a = 101 \text{ s}^{-1}$  (red lines), 10 atm  $a = 107.6 \text{ s}^{-1}$  (blue lines), and 100 atm,  $a = 3000 \text{ s}^{-1}$  (black lines). (For interpretation of the references to color in this figure legend, the reader is referred to the web version of this article.)

species concentrations, and reaction rates are examined over a broad range of strain rates and pressures. Figure 10 shows the temperature distributions at three different pressures and strain rates. Although the flame thickness and maximum flame temperature for the three cases are quite different, due to the combined effect of pressure and strain rate, they bear intrinsic similarities. To this end, we first align the flames by shifting the location of the maximum flame temperature to  $x = 0$ , normalize the  $x$ -coordinate by

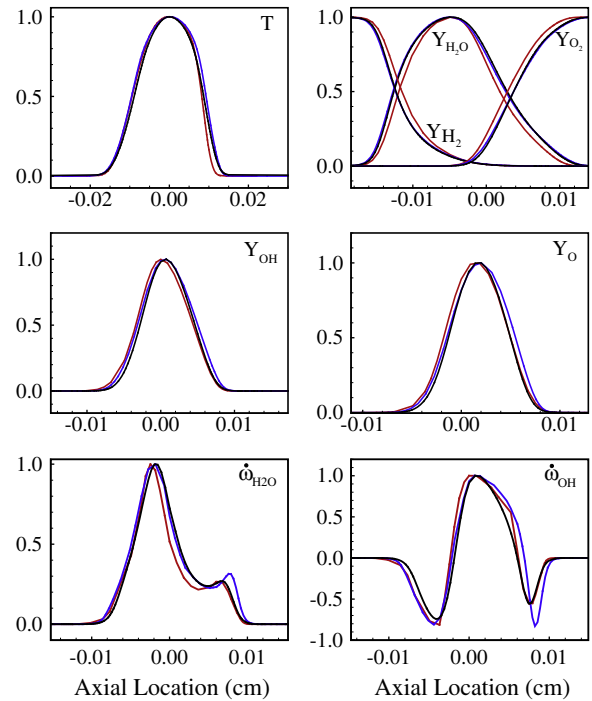


**Fig. 11.** Normalized flame temperature, mass fractions and reaction rates at different pressures and strain rates, 1 atm  $a = 101 \text{ s}^{-1}$  (red lines), 10 atm  $a = 107.6 \text{ s}^{-1}$  (blue lines), and 100 atm,  $a = 3000 \text{ s}^{-1}$  (black lines). (For interpretation of the references to color in this figure legend, the reader is referred to the web version of this article.)

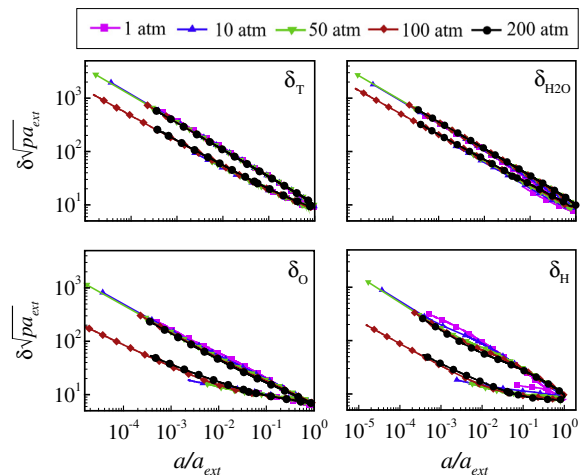


**Fig. 12.** Normalized flame thickness based on half maximum width of temperature and mass fractions of  $\text{H}_2\text{O}$ , OH and H as functions of normalized strain rate ( $a/a_{ext}$ ) at different pressures.

$\bar{T}^{0.75} / \sqrt{p a}$ , and then normalize the flame property of interest with respect to its maximum value for a given flame. The results are given in Fig. 11. The normalized profiles of temperature, mass fractions of  $\text{H}_2\text{O}$ , OH, and H, and reaction rates of  $\text{H}_2\text{O}$  and OH are almost identical for different pressures and strain rates. A strong similarity in the flame profiles exists, especially for pressures greater than 10 atm.

Figures 10 and 11 show the results of only three selected strain rates and pressures. It is desirable, however, to confirm the similarities of flame structures over a wide range of flow conditions. Figure 12 presents four different types of flame thickness,  $\delta$ , defined based on the half maximum width of the temperature

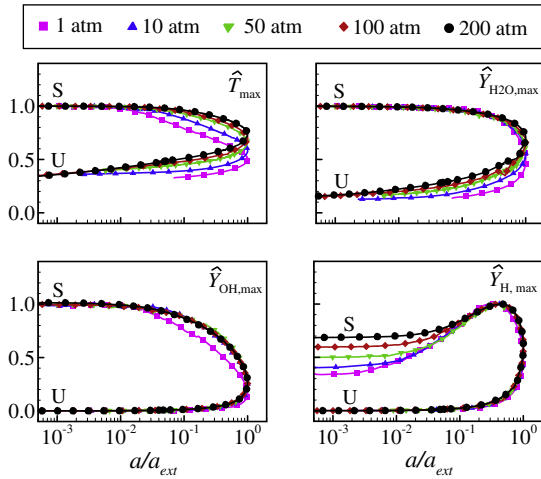


**Fig. 13.** Normalized maximum temperature and mass fractions of H<sub>2</sub>O, OH, and H in the flame as functions of normalized strain rate ( $a/a_{ext}$ ) at different pressures. S: stable burning branch, U: unstable burning branch.

and mass fractions of H<sub>2</sub>O, OH and H, respectively, as functions of the normalized strain rate  $a/a_{ext}$ . The pressure covers a range of 1–200 atm, and the flame thickness is scaled by  $1/\sqrt{p a_{ext}}$ . Identical profiles for the flame thickness are obtained over the entire S-curve.

The flame structures feature a similar trend for temperature and species. Figure 13 shows the maximum temperature and mass fractions of combustion products in the flame zone as functions of the normalized strain rate  $a/a_{ext}$ . All the flame quantities are normalized with respect to their largest values over the entire S-curve. For example, the maximum flame temperature is normalized by its highest value at the limit of zero strain rate. The normalized maximum flame temperatures for various pressures fall onto a single profile at low strain rates, but start to deviate at larger strain rates ( $0.1 a_{ext}$  for high pressures and  $0.01 a_{ext}$  for 1 atm). The H<sub>2</sub>O and OH mass fractions exhibit strong similarities for the stable burning branch of the S-curve, except for the 1 atm case. The situation with the H radical, however, is quite different. The largest value of the maximum H mass fraction in a flame ( $Y_{H,max}$ ) occurs at a high strain rate, and the normalized profiles collapse for  $a/a_{ext} > 0.1$ . For low strain rates ( $a/a_{ext} < 0.01$ ),  $Y_{H,max}$  profiles are flat at all pressures. A careful examination of  $Y_{H,max}$  profiles suggests a different scaling strategy. For each pressure,  $Y_{H,max}$  can be renormalized in terms of two extreme values over the stable burning branch,  $(Y_{H,max})_S$  and  $(Y_{H,max})_L$  as follows:

$$\hat{Y}_{H,max} = \frac{Y_{H,max} - (Y_{H,max})_S}{(Y_{H,max})_L - (Y_{H,max})_S}, \quad (18)$$

where the subscripts S and L outside the parentheses denote the smallest and largest values on the upper branch of the S-curve, respectively. The scaled  $\hat{Y}_{H,max}(p)$  at different pressures have different profiles, but all the profiles can be expressed as the sum of the profile at 1 atm and a Gaussian distribution as follows:

$$\hat{Y}_{H,max}(p) = \hat{Y}_{H,max}|_{1atm} + G(p), \quad (19)$$

where

$$G(p) = \frac{C}{\sqrt{2\pi}\sigma} \exp\left\{-\frac{[\log(a/a_{ext}) - \mu]^2}{2\sigma^2}\right\}, \quad (20)$$

The mean and standard deviation are  $\mu = -1.4$  and  $\sigma = 0.8$ , respectively. The coefficient C is a function of pressure,

$$C = 0.46 - 0.636 \log(p/p_0) \text{ with } p_0 = 1 \text{ atm}. \quad (21)$$

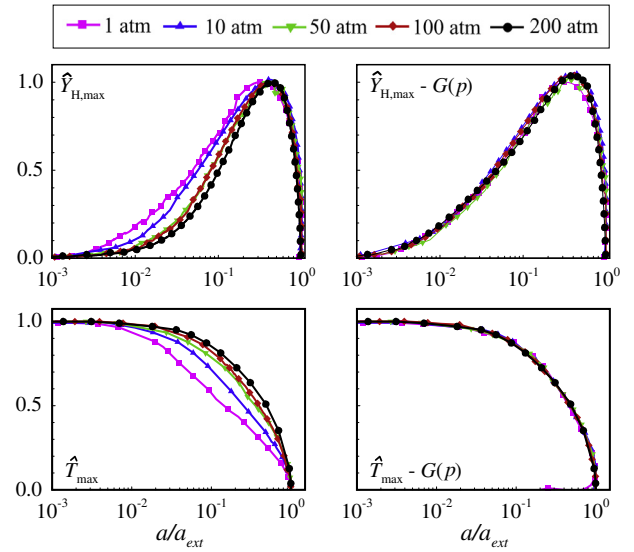


**Fig. 14.** Renormalized maximum mass fraction of H radical,  $\hat{Y}_{H,max}$ , and temperature,  $\hat{T}_{max}$ , in the flame zone.

Figure 14 shows  $\hat{Y}_{H,max}(p)$  and  $\hat{Y}_{H,max}(p) - G(p)$ . The scaling given by Eq. (19) collapses the results at various pressures and strain rates perfectly.

Similarly, the maximum flame temperature can be scaled as

$$\hat{T}_{ax} = \frac{T_{max} - (T_{max})_S}{(T_{max})_L - (T_{max})_S}, \quad (22)$$

where  $(T_{max})_S$  and  $(T_{max})_L$  represent the smallest and largest maximum flame temperature on the upper branch of the S-curve.  $\hat{T}_{max}(p)$  can be correlated with the profile at 200 atm and a Gaussian distribution in the following form

$$\hat{T}_{max}(p) = \hat{T}_{max}|_{200atm} + G(p), \quad (23)$$

where the standard deviation  $\sigma$  remains 0.8 for all pressure conditions, but the mean  $\mu$  and the coefficient C are pressure-dependent, as listed in Table 2.  $\hat{T}_{max}(p)$  and  $\hat{T}_{max}(p) - G(p)$  are also shown in Fig. 14. The maximum temperature profiles at different pressures thus become identical. Consequently, correlations for flame solutions at different pressures can be established for all species concentrations, as well as the flame temperature. Results for a given pressure can thus be mapped from those at another pressure.

Figure 15 shows the maximum reaction rates for different species, normalized by their respective highest values over the entire S-curve, as a function of normalized strain rate. Almost all the curves collapse, except for slight deviations at low pressures for the unstable burning branch.

Detailed flame information at a given pressure can be mapped to another through the scaling relationships discussed above. With this general flame similarity, the database size for chemistry tabulation can be significantly reduced, provided the reference quantities (either at the equilibrium states with low-strain rates, or close to the extinction points) are available for normalizations. Figure 16 shows the maximum flame temperature and mass fractions of H<sub>2</sub>O,

**Table 2**  
Scaling constants for renormalization of maximum flame temperature.

$p$ , atm	$C/\sqrt{2\pi}$	$\mu$
1	-0.5	0.8
10	-0.3	0.65
50	-0.15	0.6
100	-0.05	0.15

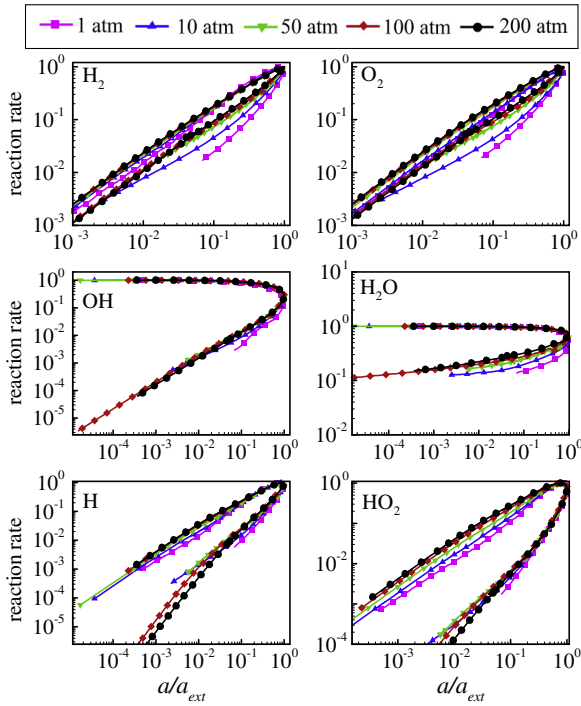


Fig. 15. Normalized rates of production of species as functions of normalized strain rate ( $a/a_{ext}$ ) at different pressures.

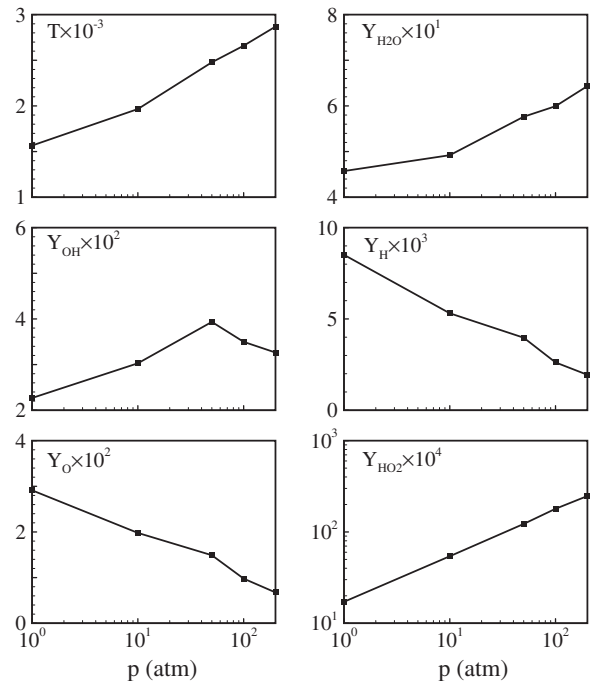


Fig. 17. Maximum values of flame temperature and species mass fractions as functions of pressure at extinction strain rate.

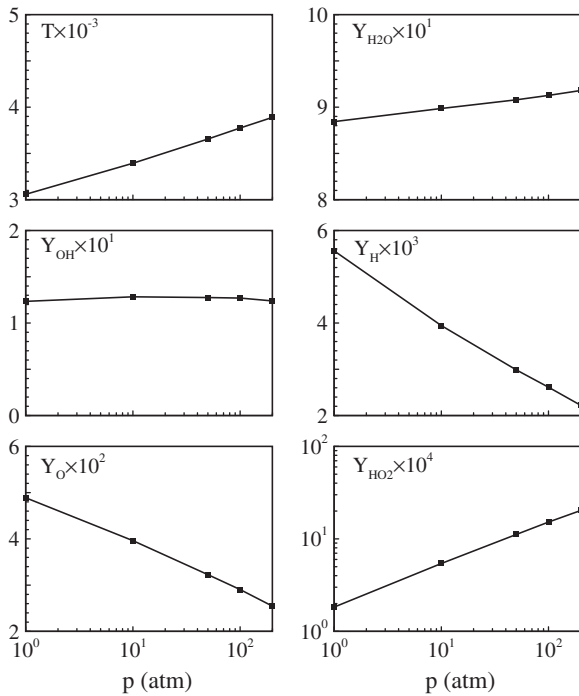


Fig. 16. Maximum values of flame temperature and species mass fractions as functions of pressure at chemical equilibrium conditions.

OH, O, H, HO<sub>2</sub>, and H<sub>2</sub>O<sub>2</sub> at the chemical equilibrium state (zero strain rate) as a function of pressure. Linear relationships are obtained for all variables on either a semi-log or a log–log scale. The increase of the flame temperature with pressure may be attributed to the suppression of dissociation reactions at high pressures. The maximum mass fraction of OH remains almost independent of pressure. Figure 17 shows the maximum values of flame properties

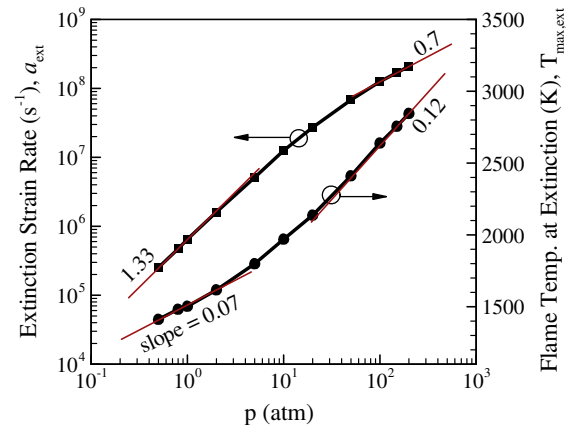


Fig. 18. Extinction strain rate,  $a_{ext}$ , and flame temperature,  $T_{max,ext}$ , as functions of pressure.

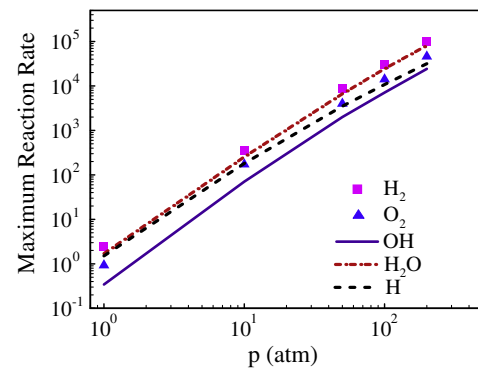


Fig. 19. Maximum reaction rates for several different species as functions of pressure.

at extinction strain rates. Results bear close similarity to those at the equilibrium state (see Fig. 16).

Figure 18 shows the strain rates and flame temperatures at the extinction points over a pressure range of 0.5–200 atm. The extinction strain rate increases almost linearly with pressure on a log–log scale  $a_{ext} \sim p^{1.33}$ , for  $p \leq 10$  atm. The relationship becomes less pressure dependent at high pressures with  $a_{ext} \sim p^{0.7}$ . The extinction flame temperature can be approximately scaled with pressure in the form  $T_{f,ext} \sim p^{0.07}$  for  $p \leq 2$  atm, and  $T_{f,ext} \sim p^{0.12}$  for higher pressures.

At the extinction point, the chemical and flow time scales are of the same order of magnitude, and the flame is kinetics-controlled.

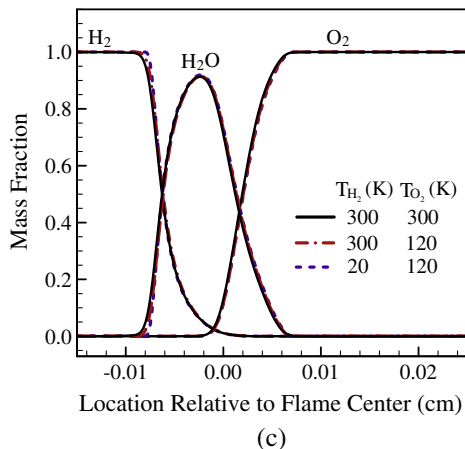
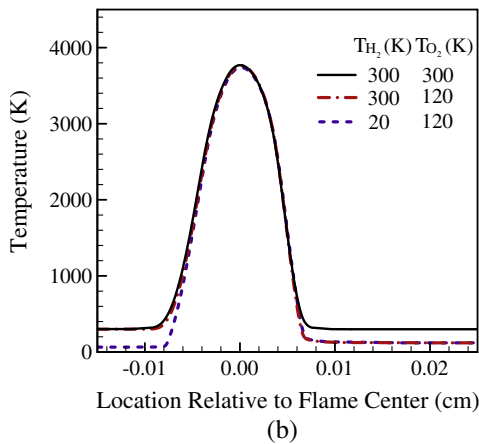
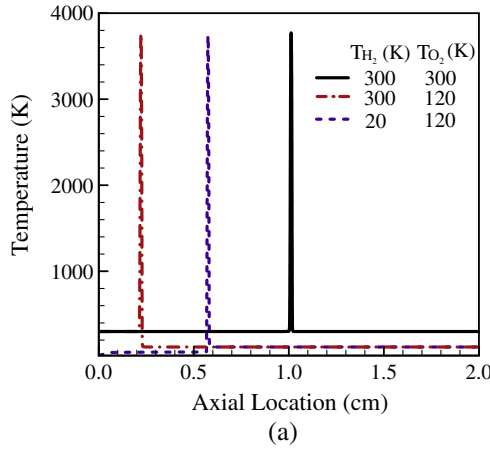


Fig. 20. Distributions of temperature and mass fractions of major for different inlet temperatures,  $p = 100$  atm,  $a = 20,004 \text{ s}^{-1}$ .

The present analysis shows that the dependence of the reaction order,  $n$ , on pressure has a value of 2.2 for  $p \leq 5$  atm. It decreases to 1.7 at high pressures. If we assume that the molecular weight of reaction products  $MW_{mix}$  is independent of pressure, and  $\bar{h}$  is linearly proportional to  $\bar{T}$ , with some straightforward manipulations, Eq. (14) becomes:

$$a_{ext} \sim \frac{\bar{\omega}}{\rho} \sim \bar{T} p^{n-1}. \quad (24)$$

Substitution of the pressure dependence of the flame temperature leads to  $a_{ext} \sim p^{1.3}$  at 0.5 atm and  $a_{ext} \sim p^{0.8}$  at 200 atm. The correlation shown in Fig. 18 is thus derived analytically. The extinction strain rate  $a_{ext}$  at a given pressure can be estimated based on the value at 1 atm, in accordance with Eq. (24). For hydrogen and oxygen flames, approximately,  $a_{ext} \sim p$  over the entire pressure range considered in the present study.

Figure 19 shows the maximum reaction rates for selected species over the entire S-curve in the pressure range of 1–200 atm. The information is used to normalize the reaction rates in Fig. 13. The slopes for  $\text{O}_2$ ,  $\text{H}_2$ ,  $\text{H}_2\text{O}$  and  $\text{OH}$  are almost the same, with an approximate value of 2.0. The increase of reaction rate renders the flame increasingly resistant to flow strain at high pressures. The decreased slope for  $\text{H}$  with increasing pressure may be attributed to the suppressed dissociation reactions at high pressures.

### 3.3. Effect of inlet condition

Figure 20a shows the flame structures at 100 atm with different inlet temperatures in both the subcritical and supercritical regimes. The difference in the flame location results from the variation of the inlet velocity for a given strain rate of  $a = 20,000 \text{ s}^{-1}$ . To facilitate comparison, the flames are aligned by shifting the location of the maximum flame temperature to  $x = 0$ . The result is shown in Fig. 20b and c for the temperature and species mass fraction distributions, respectively. The difference in maximum flame temperature among the three cases appears to be very small. The first case ( $T_{\text{H}_2} = T_{\text{O}_2} = 300 \text{ K}$ ) features a slightly wider flame and a higher maximum flame temperature (3771 K), while the third case ( $T_{\text{H}_2} = 20 \text{ K}$ ,  $T_{\text{O}_2} = 120 \text{ K}$ ) has the smallest flame thickness and lowest maximum flame temperature (3740 K). The second case ( $T_{\text{H}_2} = 300 \text{ K}$ ,  $T_{\text{O}_2} = 120 \text{ K}$ ) has a maximum flame temperature of 3764 K.

Figure 21 shows the effect of the strain rate on the flame temperature at  $p = 100$  atm. The decrease of the oxygen inlet temperature from 300 to 120 K has only a small effect on the flame temperature (less than 10 K), over the entire S-curve.

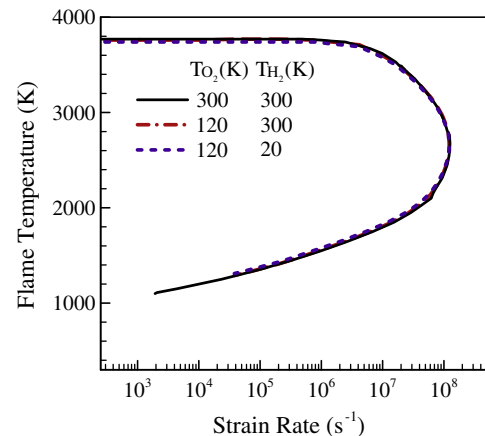


Fig. 21. Maximum flame temperature for two different oxygen inlet temperatures:  $p = 100$  atm,  $T_{\text{H}_2} = 300 \text{ K}$ .

#### 4. Conclusions

A general study has been performed to explore the effect of strain rate on counterflow diffusion flames for real fluids over the entire thermodynamic regime. The work covers all three burning branches of an S-curve. The formulation accommodates fundamental thermodynamics and transport theories, along with detailed chemical mechanisms. As a specific example, oxygen/hydrogen flames were systematically investigated for pressures in the range of 0.5–200 atm and strain rates of  $10^2$ – $10^8$  s<sup>-1</sup>. The major conclusions are as follows.

1. An analytical model was developed to corroborate and refine a previously observed relationship between the heat-release rate and pressure and strain rate in the form of  $\dot{q} \sim p^{0.534} \sqrt{a}$ . The heat release rate, when normalized with respect to  $p^{0.534} \sqrt{a_{ext}}$ , correlates well with the normalized strain rate ( $a/a_{ext}$ ).
2. As suggested by the heat-release relationship, intrinsic flame similarities are demonstrated for such properties as flame temperature, flame thickness, species concentrations, reaction rates, and heat release rate at different pressures. These properties, when normalized properly, collapse to single profiles in the normalized strain-rate space ( $a/a_{ext}$ ).
3. The extinction strain rate, a major reference parameter in the flame similarity analysis, is clearly identified. It exhibits a quasi-linear relationship with pressure, a phenomenon which can also be explained analytically. Tabulation of pressure-dependent flame properties can be achieved by mapping the flame solution at a given pressure, according to the correlations in the normalized strain-rate space, even if the extinction strain rate is not available beforehand. This will significantly improve computational efficiency for combustion models using tabulated chemistry, such as the flamelet, FGM, and FPI models.
4. Cryogenic inlet temperature appears to affect only the flame location, and has a negligible effect on the flame structure over the entire S-curve. Consequently, the ideal-gas flame solutions can be used for fluids at supercritical conditions.

#### Acknowledgments

This work was sponsored by the Air Force Office of Scientific Research under Grant No. FA-9550-10-1-0179. The authors

gratefully acknowledge support and encouragement from Dr. Mitat A. Birkan.

#### References

- [1] C.K. Law, *Combustion Physics*, Cambridge University Press, Cambridge, NY, 2006.
- [2] N. Peters, *Turbulent Combustion*, Cambridge University Press, Cambridge, England, 2000.
- [3] V. Yang, W.E. Anderson, *Liquid rocket engine combustion instability*, vol. 169, Prog. Astro. Aero., Washington, DC, 1995. AIAA.
- [4] T.C. Lieuwen, V. Yang, *Combustion instabilities in gas turbine engines: operational experience, fundamental mechanisms and modeling*, vol. 210, Prog. Astro. Aero., Reston, VA, 2005.
- [5] A. Linan, *Acta Astronaut.* 1 (1974) 1007–1039.
- [6] G. Dixon-Lewis, T. David, P. Gaskell, S. Fukutani, H. Jinno, J. Miller, et al., *Proc. Combust. Inst.* 20 (1985) 1893–1904.
- [7] R.J. Kee, J.A. Miller, G.H. Evans, G. Dixon-Lewis, *Proc. Combust. Inst.* 22 (1989) 1479–1494.
- [8] H. Chelliah, C. Law, T. Ueda, M. Smooke, F. Williams, *Proc. Combust. Inst.* 23 (1991) 503–511.
- [9] V. Giovangigli, M.D. Smooke, *Combust. Sci. Technol.* 53 (1987) 23–49.
- [10] H.B. Keller, in: P.H. Rabinowitz (Ed.), *Applications of Bifurcation Theory*, Academic Press, New York, 1977, p. 389.
- [11] M. Nishioka, C.K. Law, T. Takeno, *Combust Flame.* 104 (1996) 328–342.
- [12] H. Pitsch, *FlameMaster*, A C++ Computer Program for 0D Combustion and 1D Laminar Flame Calculations, Tech. Rep., University of Technology (RWTH) Aachen, 1998.
- [13] R. Kee, R. Rupley, J. Miller, M. Coltrin, J. Grcar, E. Meeks, et al., *CHEMKIN-PRO*, CHEMKIN-PRO, San Diego, CA, 2008.
- [14] V. Yang, *Proc. Combust. Inst.* 28 (2000) 925–942.
- [15] G. Ribert, N. Zong, V. Yang, L. Pons, N. Darabiha, S. Candel, *Combust. Flame.* 154 (2008) 319–330.
- [16] N. Darabiha, S.M. Candel, V. Giovangigli, M.D. Smooke, *Combust. Sci. Technol.* 60 (1988) 267–285.
- [17] L. Pons, N. Darabiha, S. Candel, G. Ribert, V. Yang, *Combust Theor Model* 13 (2009) 57–81.
- [18] G. Lacaze, J.C. Oefelein, *Combust Flame* 159 (2012) 2087–2103.
- [19] N. Zong, V. Yang, *Proc Combust Inst* 31 (2007) 2309–2317.
- [20] H. Meng, V. Yang, *J Comput Phys* 189 (2003) 277–304.
- [21] N. Zong, H. Meng, S.Y. Hsieh, V. Yang, *Phys Fluids* 16 (2004) 4248–4261.
- [22] N. Zong, V. Yang, *Combust Sci Technol* 178 (2006) 193–227.
- [23] N. Zong, V. Yang, *Proc Combust Inst* 31 (2007) 2309–2317.
- [24] G. Soave, *Chem Eng Sci* 27 (1972) 1197–1203.
- [25] T.H. Chung, M. Ajlan, L.L. Lee, K.E. Starling, *Ind Eng Chem Res* 27 (1988) 671–679.
- [26] S. Takahashi, *J Chem Eng Jpn* 7 (1975) 417–420.
- [27] H. Meng, G.C. Hsiao, V. Yang, J.S. Shuen, *J Fluid Mech* 527 (2005) 115–139.
- [28] J. Li, Z.W. Zhao, A. Kazakov, F.L. Dryer, *Int J Chem Kinet* 36 (2004) 566–575.
- [29] B.E. Poling, J.M. Prausnitz, J.P. O'Connell, *The Properties of Gases and Liquids*, fifth ed., McGraw-Hill, New York, 2001.
- [30] T. Poinot, D. Veynante, *Theoretical and Numerical Combustion*, second ed., Edwards, Philadelphia, 2005.